Discrete-Time Super-Twisting Sliding Mode Current Controller With Fixed Switching Frequency for Switched Reluctance Motors

Filipe P. Scalcon, *Student Member, IEEE*, Gaoliang Fang, *Member, IEEE*, Rodrigo P. Vieira, *Member, IEEE*, Hilton A. Gründling, *Member, IEEE*, and Ali Emadi, *Fellow, IEEE*

***Abstract*—This article proposes a discrete-time super-twisting sliding mode (DTSTSM) current controller for switched reluctance motors. A novel gain design procedure is proposed, guaranteeing a systematic and straightforward design stage. The method makes use of a cost function, enabling the gains that yield the best trade-off between reference tracking and low current ripple to be determined. The procedure is repeated for different speed values, allowing for a variable gain structure, where the controller gains are adjusted online based on the rotor speed. The proposal presents a simple structure, not requiring knowledge of the machine parameters during implementation, along with a pulsewidth modulation scheme, ensuring a fixed switching frequency. The DTSTSM controller is obtained from a discrete-time model and stability analysis is developed using a Lyapunov approach, taking into account the one sample implementation delay present in digital control applications. Experimental results are provided to demonstrate the effectiveness of the proposed approach, where a conventional hysteresis controller is used as a benchmark. Results show that the proposal is able to deliver adequate reference tracking while using significantly lower sampling frequencies. Moreover, when compared to the hysteresis controller, superior tracking is observed at low speeds, while maintaining a similar level of computational complexity.**

***Index Terms*—Current control, discrete-time control, stability, super-twisting sliding mode control, switched reluctance motor.**

I. Introduction

SWITCHED reluctance motors (SRMs) have gained interest in the past couple of decades, emerging as an alternative for already established electrical machines, such as induction and permanent magnet machines. SRMs present a simple structure, robustness, straightforward manufacturing process, and are inherently fault tolerant. Additionally, the lack of windings or permanent magnets in the rotor structure is one of its main advantages, driving down the cost of the machine [1]–[4]. It, however, presents significant challenges such as a highly nonlinear behavior, high torque ripple, and acoustic noise [1]. Torque ripple can be reduced with the use of torque sharing functions (TSFs), a technique that allows a constant torque to be produced by generating adequate current references for each active phase. The performance of such strategy, however, relies on accurate current controllers [5].

Hysteresis control is the most commonly used strategy for the current control of SRMs, due to its simplicity and independence of the model [1], [6]. This technique also presents advantages such as fast dynamic response, high robustness, and lack of sensitivity for parametric variations. However, it presents drawbacks such as a variable switching frequency, due to the varying phase inductance. Moreover, during digital implementation, sampling limitations lead to higher current ripple and, consequently, torque ripple. These issues are significantly more noticeable in low-speed conditions and in SRMs with low inductance values. Increasing the sampling frequency can be used to improve the performance of hysteresis controllers, reducing the current ripple [7]. However, it also tends to increase the cost of the overall control system.

In order to avoid the aforementioned issues, SRM current control strategies with fixed switching frequency have been investigated in the past few years [8], [9]. An adaptive pulsewidth modulation (PWM) current controller is detailed in [10]. The proposal makes use of online gain adaptation, warranting robustness to the algorithm while ensuring suitable dynamic responses. In addition, an improved sampling method is designed, which successfully avoids the PWM delay. A variable gain proportional–integral (PI) controller is described in [11]. Gain adaptation is done with respect to current and position, aiming to ensure stability. The back electromotive force (EMF) of the motor is also taken into account to further improve the performance of the controller. These techniques are known as model-dependent, given that they make use of machine magnetization data. This information is normally stored in lookup tables, requiring knowledge of the machine parameters and significant memory allocation.

As an alternative, linearized models have also been used for designing SRM current controllers. In [12], the inductance

Manuscript received May 18, 2021; revised August 2, 2021; accepted September 23, 2021. Date of publication September 28, 2021; date of current version November 30, 2021. This work was supported in part by the Natural Sciences and Engineering Research Council of Canada (NSERC) and in part by the Coordenação de Aperfeiçoamento de Pessoal de Nível Superior – Brasil (CAPES/PROEX) Finance Code 001. Recommended for publication by Associate Editor K.-B. Lee. *(Corresponding author: Gaoliang Fang.)*

Filipe P. Scalcon, Rodrigo P. Vieira, and Hilton A. Gründling are with Power Electronics and Control Research Group, Federal University of Santa Maria – UFSM, Santa Maria 97105-900, Brazil (e-mail: filipescalcon1@gmail.com; rodrigovie@gmail.com; ghilton03@gmail.com).

Gaoliang Fang and Ali Emadi are with McMaster Automotive Resource Center, McMaster University, Hamilton, ON L8P0A6, Canada (e-mail: fangg3@mcmaster.ca; emadi@mcmaster.ca).

Color versions of one or more figures in this article are available at https://doi.org/10.1109/TPEL.2021.3116096.

Digital Object Identifier 10.1109/TPEL.2021.3116096

characteristics of the SRM are utilized in order to build a small signal model, which is subsequently employed in the design process of a fixed-gain PI controller. A back-EMF estimation algorithm is also developed and used as a feedforward action. The performance of the controller is comparable to a variable gain PI with compensation. Strategies based on model predictive control (MPC) are presented in [13]–[16]. Continuous control set MPC benefits from a fixed switching frequency, as opposed to finite control set MPC. The technique presents advantages of fast dynamic responses, an optimal control law, and is capable of encompassing nonlinearities in the predictive model. On the flip side, it typically presents high computational burden [16].

The use of sliding mode algorithms for SRMs has been reported in [17] and [18]. The technique is desirable as it delivers robustness, while also enabling PWM implementation. An adaptive sliding mode controller based on a linear SRM model is presented in [17]. In [18], an integral sliding mode current controller with constant switching frequency is proposed. The design is carried out based on the equivalent circuit of the SRM, and a stability analysis is presented with known and bounded uncertain motor parameters. Experimental results show that the proposal has a similar response to a higher sampling hysteresis controller, with advantages such as a lower sampling rate and fixed switching frequency. The algorithm is developed in continuous time and no discrete-time stability is discussed. The technique has been successfully extended to mutually coupled SRMs in [19] and [20].

The main drawback of discrete-time sliding mode controllers is an effect known as chattering, an oscillation of finite amplitude and frequency. Higher order sliding modes, such as the super-twisting algorithm [21], are successful at circumventing this issue without notable compromises [22], [23]. In [24], a second-order sliding mode (SOSM) current controller for SRMs is implemented. A fixed-gain structure is used and no stability analysis is presented. Recently, a SOSM current controller was proposed in [25]. The authors compare it to a traditional sliding mode approach, with the proposal showing superior performance, especially regarding chattering. It is noted, however, that no attempt of a super-twisting controller has been presented in the literature regarding SRM current control.

This article presents as a main contribution a novel discrete-time super-twisting sliding mode (DTSTSM) current control scheme for SRMs. The proposed controller presents robustness, while maintaining a simple structure, not requiring any knowledge of the machine parameters on implementation. In addition, the proposal presents enhanced tracking performance, delivering lower current and torque ripple, especially in the low to medium speed range. The strategy is implemented with the use of PWM, ensuring a fixed switching frequency. The stability analysis is investigated by means of a Lyapunov approach and, unlike what has been previously reported in the literature, the digital control implementation delay is taken into account, through an augmented model. One difficulty of super-twisting sliding mode controllers is the appropriate gain selection. To overcome this issue and guarantee a systematic and straightforward design stage, a third contribution is given by a novel gain design procedure, where a cost function is used to determine the suitable controller gains, leading to fast dynamic responses and low current ripple. The procedure is repeated for different speeds, allowing the DTSTSM controller gains to be adjusted online, according to the rotor speed. Experimental results are provided to demonstrate the effectiveness of the DTSTSM controller, where a conventional hysteresis controller is used for comparison in terms of sampling frequencies, computational complexity, current, and torque root-mean-square errors (RMSEs).

The main contributions of this article can be summarized as follows.

1) A novel DTSTSM current controller with fixed switching frequency for SRMs. Compared with other PWM-based controllers, the proposed controller does not require lookup tables or any knowledge of the machine parameters on hardware implementation, presenting a simple structure and robust performance.
2) An original stability analysis, using an augmented model that takes into account the one sample digital implementation delay.
3) A systematic and straightforward gain design procedure for super-twisting sliding mode controllers. In addition, gain adaptation is employed with respect to rotor speed, allowing improved tracking over a wide range of speed.

II. Modeling of the Switched Reluctance Motor

The SRM is excited exclusively by its stator windings [1]. By disregarding phase coupling, the voltage at the terminals of an SRM is

$$v_{ph} = Ri + \frac{d\phi}{dt} \tag{1}$$

where v_{ph} is the phase voltage, R is the winding resistance, i is the phase current, and ϕ is the flux linkage. As a result of the double salient structure of the machine, flux linkage is a nonlinear function of both current and rotor position, θ.

$$\phi(i,\theta) = L(i,\theta)i(t). \tag{2}$$

Substituting (2) in (1) and computing the derivative yields

$$v_{ph} = Ri + L(\theta,i)\frac{di}{dt} + i\frac{dL(\theta,i)}{dt}. \tag{3}$$

Expanding the inductance derivative with respect to time yields

$$\frac{dL(\theta,i)}{dt} = \frac{\partial L(\theta,i)}{\partial\theta}\frac{d\theta}{dt} + \frac{\partial L(\theta,i)}{\partial i}\frac{di}{dt}. \tag{4}$$

Substituting (4) in (3) and rewriting the terms results

$$v_{ph} = Ri + l(\theta,i)\frac{di}{dt} + \epsilon \tag{5}$$

where

$$l(\theta,i) = L(\theta,i)\frac{di}{dt} + i\frac{\partial L(\theta,i)}{\partial i} \tag{6}$$

$$\epsilon = i\omega_r\frac{\partial L(\theta,i)}{\partial\theta}. \tag{7}$$

The first term, $l(\theta,i)$, is referred to as incremental inductance [26]. It accounts for the effects of magnetic saturation, by

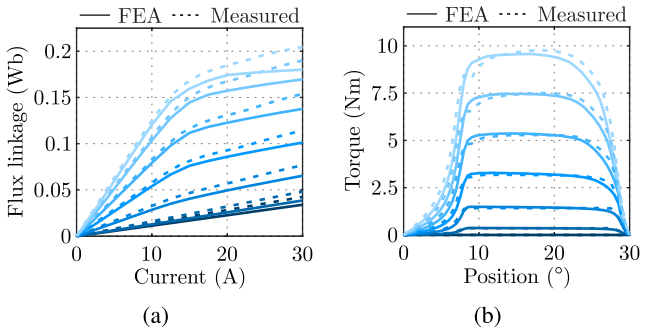

Fig. 1. Characteristics of the 8/6 studied SRM. (a) Flux linkage profile. (b) Torque profile.

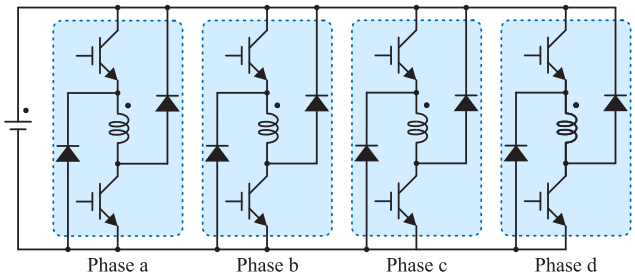

Fig. 2. Four-phase asymmetric half-bridge converter.

TABLE I
PARAMETERS OF THE STUDIED SRM

Parameter	Value
Rated speed	6000 r/min
Rated power	5.1 kW
Rated torque	8 Nm
Rated voltage	300 V
Rated current (Phase RMS value)	14.35 A
Number of phases	4
Stator poles	8
Rotor poles	6

considering current, self-inductance $L(\theta, i)$, and the inductance variation caused by current. The term ϵ corresponds to the machine's back-EMF.

A simulation model of the SRM is constructed on MATLAB/Simulink software, using lookup tables based on finite element analysis (FEA) data [1]. The flux linkage and torque profiles of the studied 8/6 SRM are presented in Fig. 1. A four-phase asymmetric half-bridge (AHB) converter, shown in Fig. 2, is used to drive the machine. Additional parameters of the machine are shown in Table I.

III. DISCRETE-TIME SUPER-TWISTING SLIDING MODE CURRENT CONTROLLER

Conventional discrete-time sliding mode control strategies exhibit chattering as a major drawback in practical applications. Chattering is a phenomenon often referred to as oscillations of finite amplitude and frequency, which occur as a result of the sliding action of the controller. This effect is undesirable as it can decrease the control accuracy and, on SRM current controllers, lead to increased current ripple [27]. The super-twisting algorithm, proposed by Levant [21], is able to effectively reduce chattering, without major compromises [22], [23]. In this section, a DTSTSM current controller for an SRM is described. A novel stability proof, considering the digital implementation delay through an augmented model, is also presented.

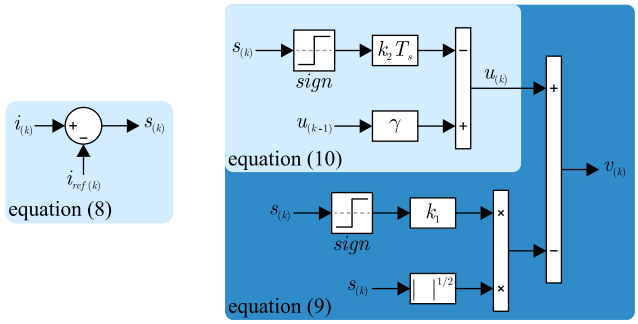

Fig. 3. Block diagram of the DTSTSM controller.

A. Controller Structure

First, consider a sliding surface, $s_{(k)}$, defined as

$$s_{(k)} = e_{(k)} = i_{(k)} - i_{ref(k)} \tag{8}$$

where $e_{(k)}$ is the current tracking error, $i_{(k)}$ is the measured phase current, and $i_{ref(k)}$ is the reference current. In accordance with [28], a DTSTSM control law can be written as

$$v_{(k)} = -k_1 \left|s_{(k)}\right|^{\frac{1}{2}} sign\left(s_{(k)}\right) + u_{(k)} \tag{9}$$

$$u_{(k)} = \gamma u_{(k-1)} - k_2 T_s sign\left(s_{(k)}\right) \tag{10}$$

where $v_{(k)}$ is the controller output, $u_{(k)}$ is the auxiliary variable of the DTSTSM controller, γ is a fixed gain with $0 < \gamma < 1$, k_1 and k_2 are the controller gains, and T_s is the sampling period.

The signal function, $sign(s_{(k)})$, is defined as

$$sign\left(s_{(k)}\right) = \begin{cases} 1 & \text{if} \quad s_{(k)} > 0 \\ 0 & \text{if} \quad s_{(k)} = 0 \\ -1 & \text{if} \quad s_{(k)} < 0. \end{cases} \tag{11}$$

A block diagram of the DTSTSM controller, described in (8)–(10), is presented in Fig. 3. Note that for implementation, the controller only requires knowledge of the gains as well as the reference and measured currents, not requiring any lookup table or additional machine parameters.

B. Stability Analysis

In digitally controlled motor drives, it is a common practice to sample the phase currents and rotor position at the same instant that the voltage commands are updated. In symmetric PWM applications, these variables are updated once per cycle, thus resulting in a intrinsic delay of T_s, as depicted in Fig. 4 [29]. If not properly addressed, this phenomenon may affect the stability of the closed-loop system.

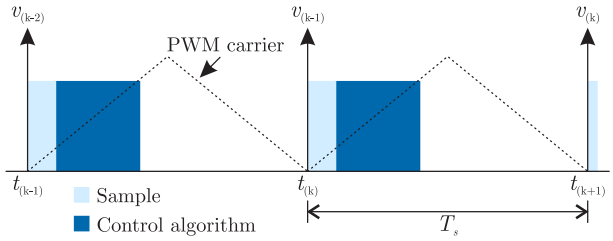

Fig. 4. Digital implementation delay in discrete-time control systems using symmetric PWM.

In order to address this issue, first, the discrete form of (5) can be obtained by using the forward Euler method, as follows:

$$i_{(k+1)} = \left(1 - T_s \frac{R}{l(\theta,i)}\right) i_{(k)} - \frac{T_s}{l(\theta,i)} \epsilon_{(k)} + \frac{T_s}{l(\theta,i)} v_{(k)}. \tag{12}$$

Next, an augmented model can be derived from (12), where an additional state, $v_{d(k)}$, is included to account for the digital control implementation delay

$$\begin{bmatrix} i_{(k+1)} \\ v_{d(k+1)} \end{bmatrix} = \begin{bmatrix} 1 - T_s \frac{R}{l(\theta,i)} & \frac{T_s}{l(\theta,i)} \\ 0 & 0 \end{bmatrix} \begin{bmatrix} i_{(k)} \\ v_{d(k)} \end{bmatrix} + \begin{bmatrix} 0 \\ 1 \end{bmatrix} v_{(k)} + \begin{bmatrix} -\frac{T_s}{l(\theta,i)} \epsilon_{(k)} \\ 0 \end{bmatrix}. \tag{13}$$

Then, considering the model presented in (13) and the controller given in (9) and (10), the nonlinear augmented system can be rewritten in the form of

$$\boldsymbol{x}_{(k+1)} = \boldsymbol{A}\boldsymbol{x}_{(k)} + \boldsymbol{B}_{(k)} s_{(k)} + \boldsymbol{\xi}_{(k)} \tag{14}$$

where

$$\begin{aligned} \boldsymbol{x}_{(k)} &= \begin{bmatrix} x_{1(k)} & x_{2(k)} & x_{3(k)} \end{bmatrix}^T \\ &= \begin{bmatrix} s_{(k)} & v_{d(k)} & u_{(k)} \end{bmatrix}^T \end{aligned} \tag{15}$$

$$\boldsymbol{A} = \begin{bmatrix} 1 - T_s \frac{R}{l(\theta,i)} & \frac{T_s}{l(\theta,i)} & 0 \\ 0 & 0 & 1 \\ 0 & 0 & \gamma \end{bmatrix} \tag{16}$$

$$\boldsymbol{B}_{(k)} = \begin{bmatrix} 0 & -k_1 \left|s_{(k)}\right|^{\frac{1}{2}} & -k_2 T_s \end{bmatrix}^T \tag{17}$$

$$\begin{aligned} \boldsymbol{\xi}_{(k)} &= \begin{bmatrix} \xi_{1(k)} & 0 & 0 \end{bmatrix}^T \\ &= \left[-\frac{T_s}{l(\theta,i)} \epsilon_{(k)} - \left(i_{ref(k+1)} - \left(1 - T_s \frac{R}{l(\theta,i)}\right) i_{ref(k)} \right) \; 0 \; 0 \right]^T. \end{aligned} \tag{18}$$

The stability of the closed-loop system, taking the one sample delay into account, is given by the following theorem.

Theorem 1: Consider the nonlinear system given in (14), with gains chosen as $k_1 > 0$, $k_2 > 0$, $0 < \gamma < 1$ and if the following linear matrix inequality (LMI) [23], [30], [31]

$$\boldsymbol{A}^T \left(\boldsymbol{P} + \boldsymbol{P}\left(\boldsymbol{\Lambda}_1 + \boldsymbol{\Lambda}_2\right)\boldsymbol{P}\right)\boldsymbol{A} - (1-\rho)\,\boldsymbol{P} + \boldsymbol{Q} \leq 0 \tag{19}$$

has a positive-definite solution $\boldsymbol{P} = \boldsymbol{P}^T > 0$ for a given $\boldsymbol{Q} = \boldsymbol{Q}^T > 0$, $\boldsymbol{\Lambda}_1 = \boldsymbol{\Lambda}_1^T > 0$, and $\boldsymbol{\Lambda}_2 = \boldsymbol{\Lambda}_2^T > 0$, then the trajectories of the system described in (14) converge asymptotically to a region centered at the origin $\mathrm{O} = \{x : \|x\|^2 < r\}$, with a radius given by

$$r = \frac{c}{\rho} \tag{20}$$

where

$$\begin{aligned} &0 < \rho < 1 \\ &c = \left(\frac{\alpha_2}{2\sqrt{\alpha_1}}\right)^2 + \alpha_3 \\ &\alpha_1 = \lambda_{\min}\left(\boldsymbol{Q}\right) > 0 \\ &\alpha_2 = \lambda_{\max}\left(\boldsymbol{Z}\right) k_1^2 \\ &\alpha_3 = \lambda_{\max}\left(\boldsymbol{Z}\right)\left(k_2 T_s\right)^2 + \lambda_{\max}\left(\boldsymbol{H}\right)\xi_{1(k)}^2 \\ &\boldsymbol{Z} = \boldsymbol{Z}^T = \boldsymbol{\Lambda}_1^{-1} + \boldsymbol{\Lambda}_3^{-1} + \boldsymbol{P} > 0 \\ &\boldsymbol{H} = \boldsymbol{H}^T = \boldsymbol{\Lambda}_2^{-1} + \boldsymbol{P}\boldsymbol{\Lambda}_3\boldsymbol{P} + \boldsymbol{P} > 0. \end{aligned}$$

The detailed proof for Theorem 1 is presented in the Appendix.

IV. Gain Design Procedure

The proper selection of a DTSTSM controller gains is necessary in order to guarantee acceptable performance and low chattering [22]. Due to the wide gain constraint intervals, traditional sliding mode control design is not an efficient approach. Moreover, for the SRM current control application, different sets of gains lead to different settling times and current ripple values. Generally, larger gains lead to faster settling times; however, they also tend to increase overshoot and current ripple. Smaller gains, on the other hand, often present a slower response along with a lower current ripple. Given the highly nonlinear behavior of the SRM, the use of analytical formulations to determine the controller gains becomes a complex task. Additionally, the back-EMF of the machine plays an important role, generally degrading the tracking capability of the controller at higher speeds [12].

In this context, an optimization-based design can be an interesting tool. Using an offline grid search algorithm allows several points of a defined search space to be evaluated, where a cost function is used to determine suitable controller gains, which present the best trade-off between reference tracking and low current ripple. Moreover, the performance of the controller can be improved by online gain adaption, with respect to the rotor speed. In the following subsections, a novel gain design procedure for a DTSTSM controller and a design example are presented, respectively.

A. Design Procedure

To guide the algorithm, a cost function, $F(k_1, k_2 T_s)$, is defined as the sum of the absolute value of the current tracking error

$$F\left(k_1, k_2 T_s\right) = \max\left(\sum_{0}^{\theta_{\text{exc}}} \left|s_{(k)}\right|\right) \tag{21}$$

where θ_{exc} is the excitation period.

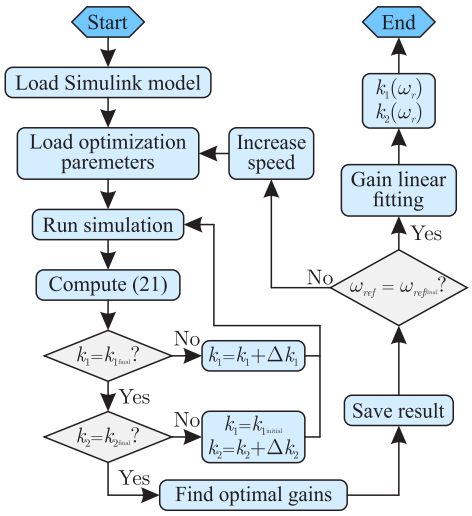

Fig. 5. Flowchart of the proposed gain design procedure.

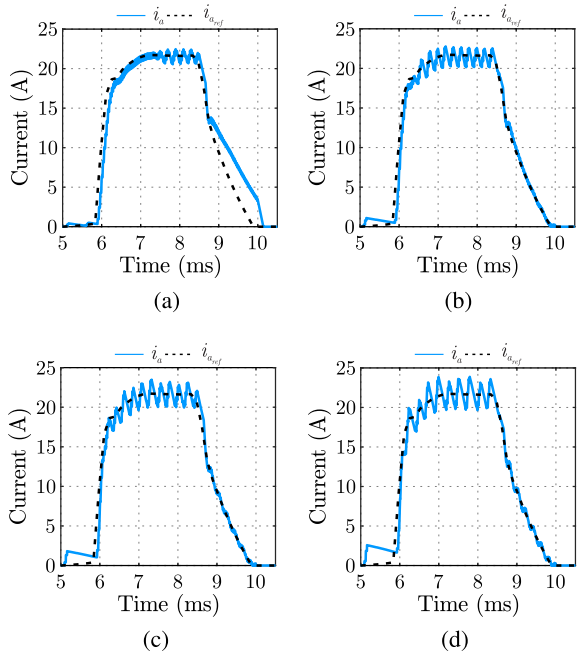

Fig. 6. Simulation results for different gain combinations at 1000 r/min with a 6 N·m load. (a) $k_1 = 50$ and $k_2T_s = 1$. (b) $k_1 = 100$ and $k_2T_s = 5$. (c) $k_1 = 150$ and $k_2T_s = 10$. (d) $k_1 = 200$ and $k_2T_s = 15$.

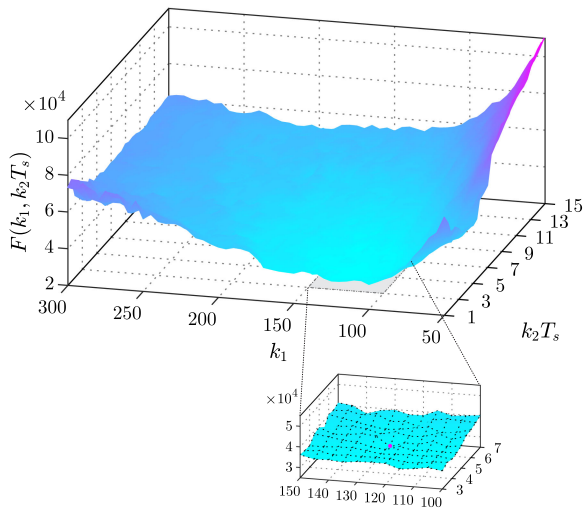

Fig. 7. Cost function values at a speed of 1000 r/min, highlighting the region of the search space containing the optimal gain combination.

This choice is made as a means to find a set of gains that present good tracking capability, with both a fast transient response and low current ripple. Note that the cost function is calculated during the excitation interval, when the reference phase current is greater than zero.

The proposed design procedure is presented in Fig. 5. The procedure is performed offline and starts with the simulation model being loaded in MATLAB/Simulink. Then, the optimization parameters are set, them being the search space and the gain increments. Following this, the simulation procedure starts, where one simulation is performed for each pair of gains. At the end of each simulation, the cost function is calculated and the value is stored. Once every simulation has been executed, the gains that yielded the lowest cost function value are stored as the optimal gains for that particular speed. Following this, the reference speed is incremented and the procedure is repeated until the every desired speed value is evaluated. Finally, a linear fitting is performed, where the optimal gains are fitted to a straight line, allowing simple digital implementation.

B. Design Example

This section aims to present a gain design example for the DTSTSM current controller using the proposed methodology, while also providing experimental validation in the following section.

Consider the 8/6 SRM with the parameters shown in Table I and Fig. 1, using the SRM model depicted in the end of Section II. The sampling and switching frequencies are set to 30 kHz, and a PWM with triangular carrier is used. The reference phase currents are generated according to the TSF presented in [32]. In this case, the search space was defined as $50 \leq k_1 \leq 300$, evaluated at $\Delta k_1 = 5$ increments, and $1 \leq k_2T_s \leq 15$, evaluated at $\Delta k_2T_s = 0.5$ increments. Simulations are performed for every gain combination inside the interval. In order to show the effects of different gain combinations, Fig. 6 presents the simulation results for four different sets of gains at a speed of 1000 r/min. Note how different gains affect tracking capability and current ripple. The cost function values for the entire search space at the same speed are presented in Fig. 7. In this case, the gains that yielded the best performance (i.e., minimize the cost function) are $k_1 = 125$ and $k_2T_s = 5$. The phase current and cost function waveforms for this set of gains, at a speed of 1000 r/min, are presented in Fig. 8.

Given that the performance of the controller can be enhanced by gain adjustment, the procedure is repeated in 500 r/min increments, until reaching the speed of 3000 r/min. After that, a linear fitting of the resulting gains is performed, allowing for simple implementation. The optimal results as well as the linear regressions are presented in Fig. 9.

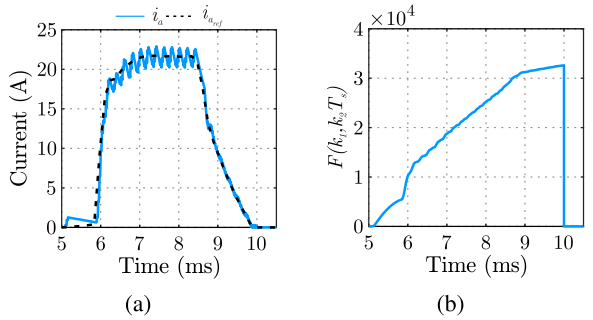

Fig. 8. Simulation results for the optimal gains at a speed of 1000 r/min. (a) Phase current. (b) Cost function.

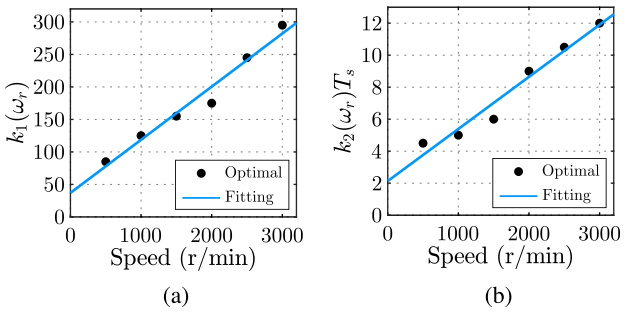

Fig. 9. Optimal gains for the proposed DTSTSM controller as a function of speed. (a) k_1. (b) $k_2 T_s$.

For digital implementation, gains k_1 and $k_2 T_s$ are calculated according to (22) and (23), respectively

$$k_1(\omega_r) = 0.08171\,|\omega_r| + 37 \tag{22}$$

$$k_2(\omega_r)\,T_s = 0.003257\,|\omega_r| + 2.133. \tag{23}$$

It is important to highlight that the proposed design procedure is carried out offline, not demanding any sort of online tuning. In addition, it must be pointed out that the gains obtained by simulation results are directly used for experimental validation, not requiring any additional design steps. Finally, note that multiple load values are not considered in the gain design procedure. This is done as a means to maintain a simple controller structure, avoiding the use of lookup tables during implementation and ensuring a faster design stage. Moreover, given the robustness of the DTSTSM controller, the above-mentioned are reasonable design choices.

V. Experimental Results

In this section, experimental tests are conducted in order to verify the effectiveness of the proposed DTSTSM current controller. The characteristics of the SRM used are presented in Fig. 1, while additional parameters of the machine are given in Table I. Fig. 10 shows the experimental test bench used to obtain the results. The setup is composed of an SRM, a four-phase AHB converter, and an induction machine (IM), coupled to the SRM. The load torque is imposed by the IM, which operates as a generator, while the SRM is controlled with predetermined current references [33].

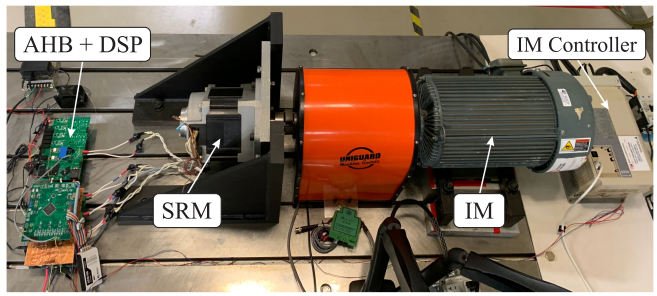

Fig. 10. Experimental test bench encompassing the drive, the SRM, and an IM, used to provide a mechanical load.

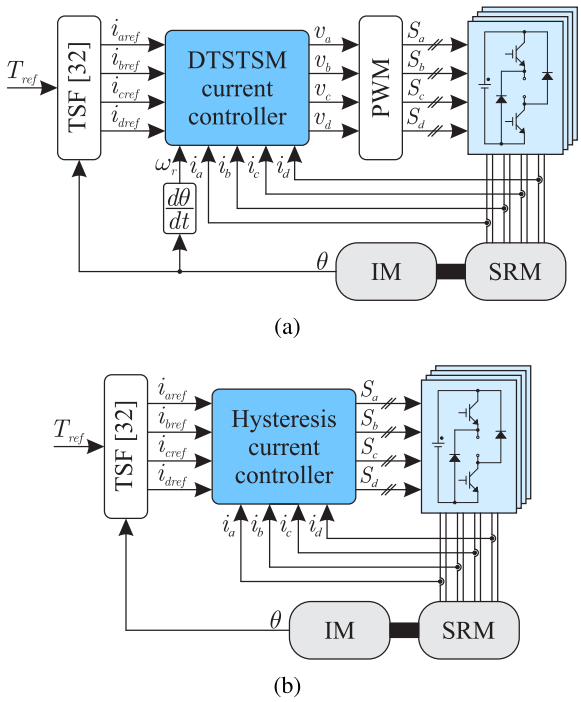

Fig. 11. Block diagram of the current control strategies. (a) DTSTSM controller. (b) Hysteresis controller.

Fig. 11(a) shows the block diagram of the proposed current control structure. A digital signal processor (DSP) TMS320F28335 is used for digital implementation. The sampling and switching frequencies are set to $f_s = f_{\text{sw}} = 30$ kHz, and a PWM with triangular carrier is used. The duty cycle used in the PWM is given by $v_{(k)}/V_{dc}$ in soft chopping mode and by $0.5 + 0.5(v_{(k)}/V_{dc})$ in hard chopping mode, where V_{dc} is the dc bus voltage [10]. The process is depicted in Fig. 12. Soft chopping is applied while $\theta < \theta_{\text{off}}$, while hard chopping is used after $\theta > \theta_{\text{off}}$, with the turn-OFF angles being stored in a lookup table. Analogous reasoning is used for hysteresis current control.

The reference phase currents are generated according to the TSF presented in [32]. For digital implementation, the DTSTSM controller gains are calculated according to (22) and (23). For comparison purposes, hysteresis current control with a hysteresis band of 1 A was applied to the same SRM, as depicted in Fig. 11(b). The sampling frequency was set to 57 kHz, the highest achievable value considering the limited performance

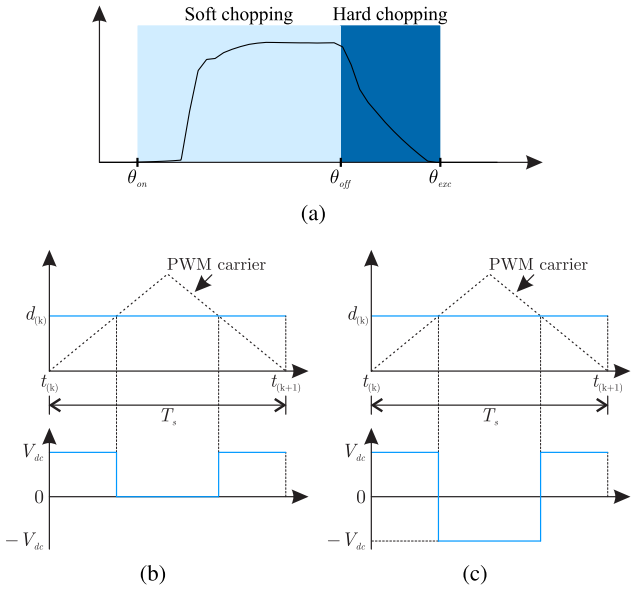

Fig. 12. PWM characteristics. (a) Current reference example with chopping regions highlighted. (b) Soft chopping waveforms. (c) Hard chopping waveforms.

of the DSP used [33]. The higher value when compared to the DTSTSM controller is chosen purposefully, allowing for a comparable performance with the proposed controller [18]. Due to digital implementation, the hysteresis controller also presents a one sample delay.

As a means to measure the tracking capability and current ripple of the proposed controller, which directly affect the torque ripple characteristic of the SRM, measurements of the current and torque RMSE are performed [18], [34]. The current and torque RMSE are defined as, respectively

$$i_{\text{RMSE}} = \sqrt{\frac{1}{N}\sum_{n=1}^{N}\left(i_{\text{ref}(k)} - i_{(k)}\right)^2} \tag{24}$$

$$T_{\text{RMSE}} = \sqrt{\frac{1}{N}\sum_{n=1}^{N}\left(T_{\text{ref}(k)} - T_{e(k)}\right)^2} \tag{25}$$

where N is the number of data points.

A. Steady-State Performance

Fig. 13 shows the experimental results for the proposed DTSTSM and hysteresis controllers under a 3 N·m load at a speed of 500 r/min. A 12-bit digital-to-analog converter is used to measure the reference current and instantaneous torque waveforms, with the latter making use of a lookup table containing characteristics of the studied SRM. It can be observed that the proposal presents a fast transient response as well as adequate reference tracking. The robustness of the proposal can also be observed, as it operates properly in the region of magnetic saturation. When compared with the hysteresis controller, significantly lower current and torque ripple are observed, while using close to a 50% smaller sampling frequency.

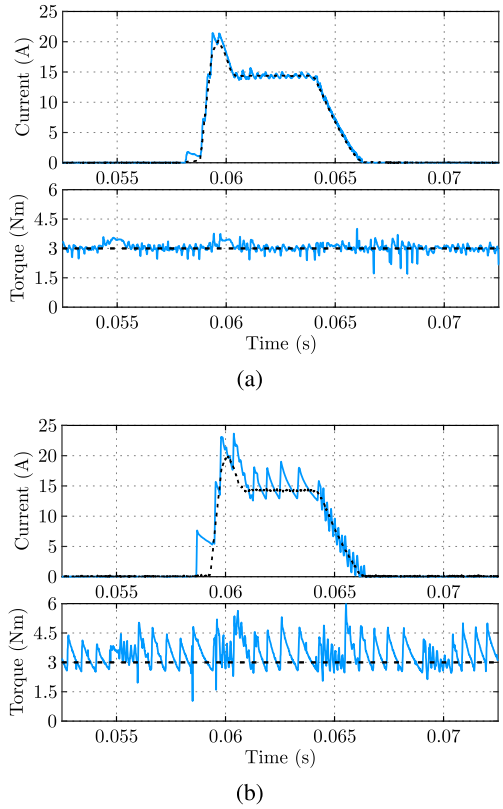

Fig. 13. Experimental results for a speed of 500 r/min and a 3 N·m load. (a) DTSTSM controller (f_s=30 kHz). (b) Hysteresis controller (f_s=57 kHz).

In order to verify the robustness of the controller to different load levels, Fig. 14 presents the experimental results for the proposed DTSTSM and hysteresis controllers under a 6 N·m load, still at a speed of 500 r/min. Once more, the proposal presents suitable tracking along with reduced current ripple. In addition, it can be seen that the controller is able to maintain the expected behavior for different load conditions, while making use of the same gains.

In order to evaluate the performance of the controllers at different speeds, experimental results for both controllers under a 6 N·m load at the speeds of 1000, 2000, and 3000 r/min are presented in Figs. 15–17, respectively. It can be seen that the proposal presents good reference tracking even at higher speeds. As an example, it can be seen that at 3000 r/min, the DTSTSM is able to present comparable tracking to the hysteresis controller, while making use of a reduced sampling rate and guaranteeing a fixed switching frequency.

A comprehensive quantitative analysis is shown in Tables II and III, where measurements of current and torque RMSE are presented for both controllers under 3 and 6 N·m loads, respectively. The tests are carried out at the speeds of 500, 1000, 2000, and 3000 r/min.

As seen in Tables II and III, the proposed controller presents smaller current and torque RMSE values across the evaluated speed range when compared to hysteresis control. It should be noted that with the increase in speed, and consequently back-EMF, the response of the hysteresis controller improves;

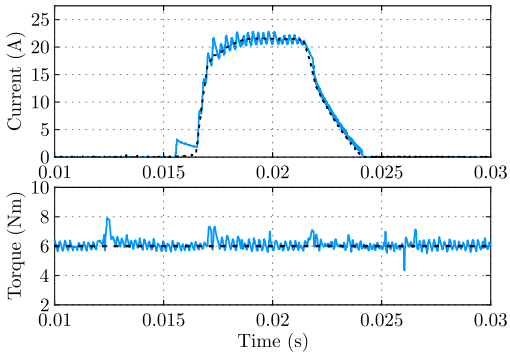

(a)

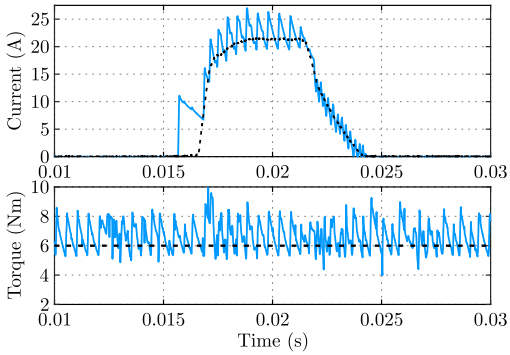

(b)

Fig. 14. Experimental results for a speed of 500 r/min and a 6 N·m load. (a) DTSTSM controller (f_s=30 kHz). (b) Hysteresis controller (f_s=57 kHz).

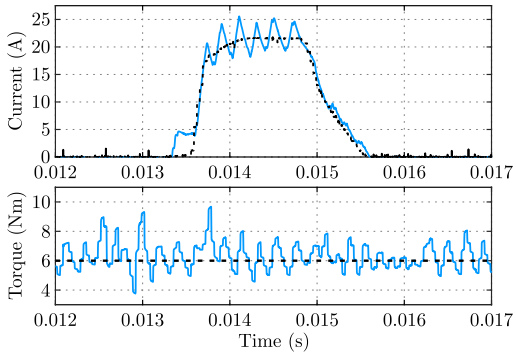

(a)

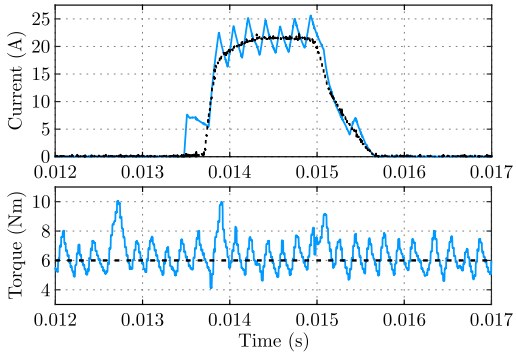

(b)

Fig. 16. Experimental results for a speed of 2000 r/min and a 6 N·m load. (a) DTSTSM controller (f_s=30 kHz). (b) Hysteresis controller (f_s=57 kHz).

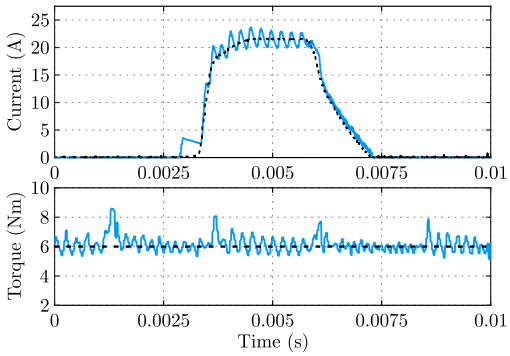

(a)

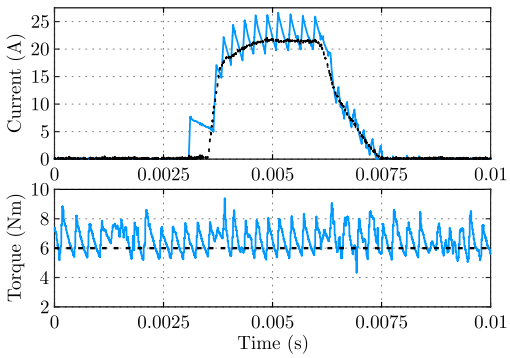

(b)

Fig. 15. Experimental results for a speed of 1000 r/min and a 6 N·m load. (a) DTSTSM controller (f_s=30 kHz). (b) Hysteresis controller (f_s=57 kHz).

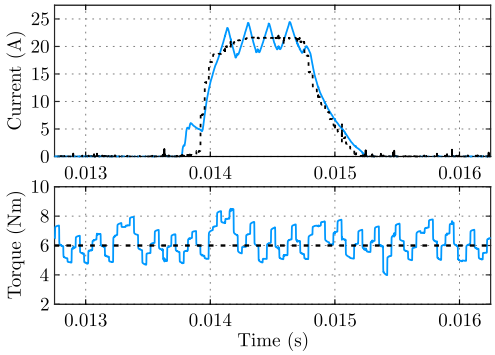

(a)

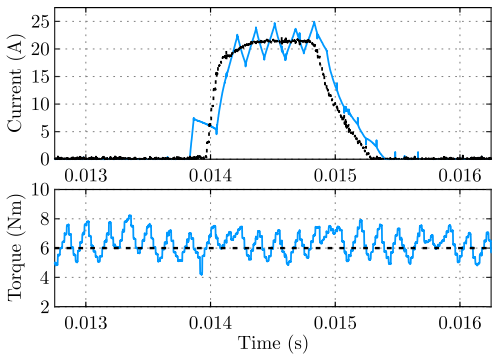

(b)

Fig. 17. Experimental results for a speed of 3000 r/min and a 6 N·m load. (a) DTSTSM controller (f_s=30 kHz). (b) Hysteresis controller (f_s=57 kHz).

TABLE II
COMPARISON OF THE DTSTSM AND HYSTERESIS CURRENT CONTROLLERS FOR A 3 N·m LOAD

Speed (r/min)	DTSTSM controller		Hysteresis controller	
	i_{RMSE} (A)	T_{RMSE} (N·m)	i_{RMSE} (A)	T_{RMSE} (N·m)
500	0.4567	0.2252	1.6515	0.7859
1000	0.6356	0.3015	1.7522	0.6859
2000	1.1098	0.6016	1.4706	0.6502
3000	1.5780	1.0626	1.9762	0.8626

TABLE III
COMPARISON OF THE DTSTSM AND HYSTERESIS CURRENT CONTROLLERS FOR A 6 N·m LOAD

Speed (r/min)	DTSTSM controller		Hysteresis controller	
	i_{RMSE} (A)	T_{RMSE} (N·m)	i_{RMSE} (A)	T_{RMSE} (N·m)
500	0.7191	0.3524	2.3321	1.1198
1000	0.9427	0.5488	2.0863	1.0270
2000	1.3433	0.9811	1.8360	1.0978
3000	1.5577	0.9820	2.5513	0.8511

however, the DTSTSM controller is still able to present a comparable performance at the speed of 3000 r/min. Moreover, the proposal has the benefit of ensuring a fixed switching frequency while also making use of a significantly lower sampling rate.

B. Dynamic Performance

As a means to further evaluate the proposal, dynamics tests are carried out. First, to evaluate the robustness to load disturbances, Fig. 18 shows the experimental results of a dynamic load test for the proposed DTSTSM and hysteresis controllers, at a speed of 500 r/min. Initially, the motor operates under a 3 N·m load, and at $t = 10$ s, the load is increased to 6 N·m.

It can be observed that the proposal presents a fast transient response as well as good disturbance rejection. Similarly to the steady-state results, significantly lower current and torque ripple are observed when compared to the hysteresis controller, while using approximately half the sampling frequency.

In order to test the performance in variable speed conditions, a dynamic speed test for the proposed DTSTSM and hysteresis controllers is presented in Figs. 19 and 20. The motor is initially controlled to 500 r/min, and then the speed is increased in a ramp until reaching 1000 r/min, under a 3 N·m load.

It is observed that the proposal presents suitable reference current and torque tracking throughout the test, including the speed variation period. Again, reduced current and torque ripple are verified when compared to the hysteresis controller.

C. Efficiency Comparison

In order to further evaluate the proposal, an efficiency comparison is carried out. The efficiency, η, is calculated as

$$\eta = \frac{P_{\text{out}}}{P_{\text{in}}} \tag{26}$$

where P_{in} is the input power and P_{out} is the output power.

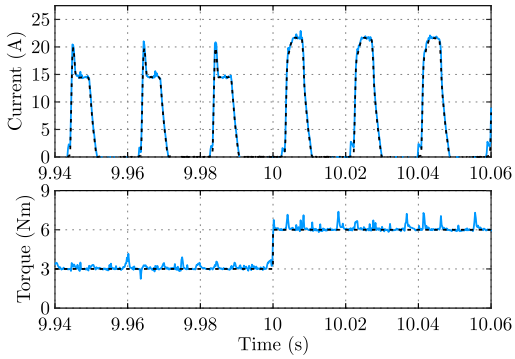

(a)

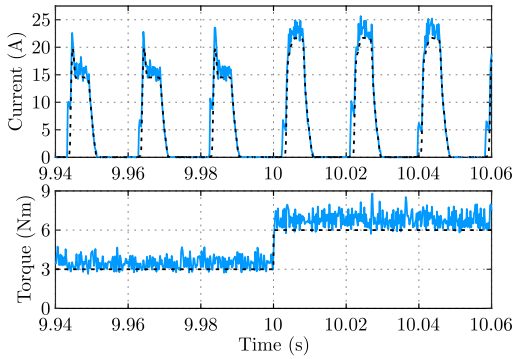

(b)

Fig. 18. Experimental results for a dynamic load condition, at a speed of 500 r/min. (a) DTSTSM controller (f_s=30 kHz). (b) Hysteresis controller (f_s=57 kHz).

TABLE IV
EFFICIENCY COMPARISON OF THE DTSTSM AND HYSTERESIS CURRENT CONTROLLERS

Speed (r/min)	3 N·m		6 N·m	
	DTSTSM controller	Hysteresis controller	DTSTSM controller	Hysteresis controller
500	47.73%	51.12%	57.79%	57.81%
1000	57.36%	62.71%	67.40%	68.27%
2000	68.84%	70.59%	75.25%	75.55%
3000	73.21%	73.94%	79.05%	79.09%

The input power is defined as

$$P_{\text{in}} = V_{\text{dc}} i_{\text{avg}} \tag{27}$$

where i_{avg} is the average dc bus current.

The output power is defined as

$$P_{\text{out}} = \omega_r T_{\text{avg}} \tag{28}$$

where T_{avg} is the average electromagnetic torque.

The efficiency results for both controllers in the operating conditions of the steady-state tests are presented in Table IV. Moreover, the RMS current values are given in Table V. The switching frequency value for the hysteresis controller varies from $f_{\text{sw}} = 1$ to 22 kHz. The proposal, as previously mentioned, presents a fixed switching frequency of $f_{\text{sw}} = 30$ kHz.

It can be seen that the DTSTSM controller presents a slightly lower efficiency, when compared to the hysteresis controller.

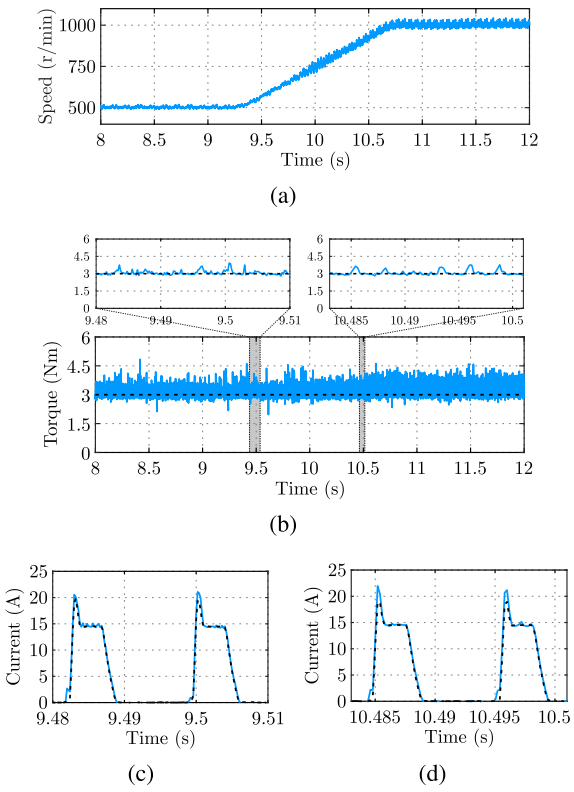

Fig. 19. Experimental results for the DTSTSM controller (f_s=30 kHz) in a variable speed condition, under a 3 N·m load. (a) Rotor speed. (b) Torque. (c) Phase current highlight 1. (d) Phase current highlight 2.

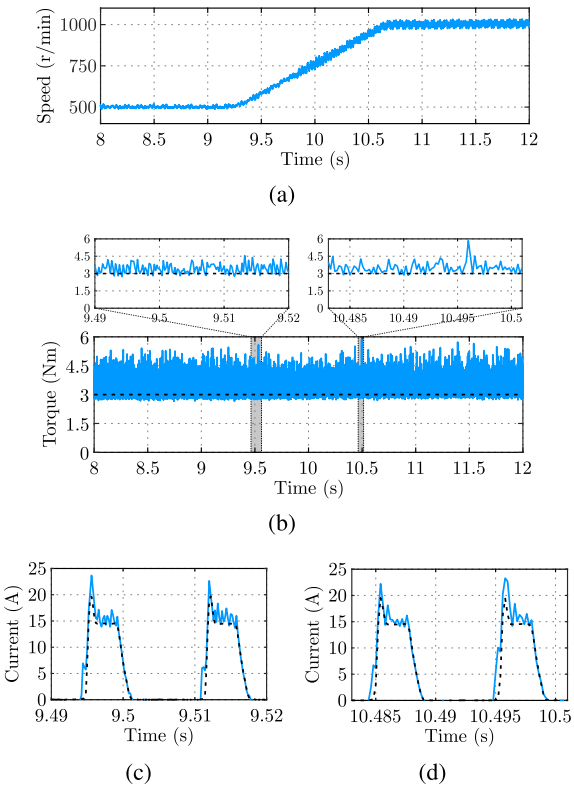

Fig. 20. Experimental results for the hysteresis controller (f_s=57 kHz) in a variable speed condition, under a 3 N·m load. (a) Rotor speed. (b) Torque. (c) Phase current highlight 1. (d) Phase current highlight 2.

TABLE V
RMS CURRENT COMPARISON OF THE DTSTSM AND HYSTERESIS CURRENT CONTROLLERS

Speed (r/min)	3 N·m		6 N·m	
	DTSTSM controller	Hysteresis controller	DTSTSM controller	Hysteresis controller
500	8.4791 A	9.0857 A	11.5301 A	12.3963 A
1000	8.6429 A	9.1585 A	11.4211 A	12.1394 A
2000	8.8416 A	8.8331 A	11.3540 A	11.8267 A
3000	8.7602 A	8.6766 A	11.4554 A	11.6424 A

TABLE VI
COMPARISON OF THE EXECUTION TIME OF THE CONTROL ALGORITHMS

Algorithm	DTSTSM	Hysteresis
Total execution time	18.44 μs	17.32 μs

From Table V, it can be observed that the proposal has overall lower RMS current values, leading to smaller copper losses. However, due to the increased switching frequency of the DTSTSM controller, the switching losses of the proposed controller are higher, leading to a slightly smaller system efficiency, more evident in the lower speed range.

D. Computational Burden Comparison

In order to evaluate the computational complexity of both controllers, a measurement of the execution time of the control algorithm is presented in Table VI. The measure takes into consideration the torque sharing as well as the current controller, with both of the controllers being tested in the same hardware and without any code optimizations. Note that only the resulting current reference waveforms from [32] are stored in the DSP, with the cumbersome reference current-generation process being carried out entirely offline. It can be observed that the DTSTSM proposal presents an execution time very similar to the hysteresis approach, meaning it presents comparable computational complexity and showing that it could be used in low-cost microcontrollers available in industry- and product-oriented applications.

VI. CONCLUSION

In this article, a DTSTSM current control scheme for SRMs is proposed. The proposal is implemented via PWM, ensuring a fixed switching frequency, while maintaining a simple structure, not requiring any knowledge of the machine parameters on implementation. A novel procedure for gain design is described, using a cost function to determine gains which ensure good tracking capability, enabling a systematic and straightforward design stage. The procedure is repeated for different speed values, allowing for a variable gain structure, where the gains are adjusted during operation based on the rotor speed. The control strategy is developed in discrete-time and the stability analysis is carried out considering the digital control implementation delay, by means of Lyapunov analysis. Experimental results show that the proposal has a comparable performance to a traditional hysteresis controller, while using a significantly lower sampling frequency and ensuring a fixed switching frequency.

Moreover, current and torque RMSE measurements attest to the good performance of the controller, showing a superior tracking performance especially at the lower speed range. Finally, the proposed controller presents a similar computational complexity to the hysteresis approach, making it a viable candidate for low-cost microcontrollers present in industry- and product-oriented applications.

APPENDIX: PROOF OF THEOREM I

Proof: The proof of Theorem 1 is based on [23], [30], and [31].

Consider the Lyapunov candidate function

$$V_{(k)} := \left\|\boldsymbol{x}_{(k)}\right\|_P^2 = \boldsymbol{x}_{(k)}^T \boldsymbol{P} \boldsymbol{x}_{(k)}. \tag{29}$$

So, $\Delta V_{(k)} = V_{(k+1)} - V_{(k)}$ can be rewritten as

$$\Delta V_{(k)} = \boldsymbol{x}_{(k+1)}^T \boldsymbol{P} \boldsymbol{x}_{(k+1)} - \boldsymbol{x}_{(k)}^T \boldsymbol{P} \boldsymbol{x}_{(k)} \tag{30}$$

where $\boldsymbol{P} = \boldsymbol{P}^T > 0$.

Replacing the augmented model, (14), in (30), results

$$\begin{aligned}\Delta V_{(k)} = {} & \left(\boldsymbol{A} x_{(k)} + \boldsymbol{B}_{(k)} \text{sign}\left(s_{(k)}\right) + \boldsymbol{\xi}_{(k)}\right)^T \boldsymbol{P} (\boldsymbol{A} x_{(k)} \\ & + \boldsymbol{B}_{(k)} \text{sign}\left(s_{(k)}\right) + \boldsymbol{\xi}_{(k)}) - \boldsymbol{x}_{(k)}^T \boldsymbol{P} \boldsymbol{x}_{(k)}.\end{aligned} \tag{31}$$

Expanding (31) results in

$$\begin{aligned}\Delta V_{(k)} = {} & \boldsymbol{x}_{(k)}^T \left(\boldsymbol{A}^T \boldsymbol{P} \boldsymbol{A} - \boldsymbol{P}\right) \boldsymbol{x}_{(k)} + \boldsymbol{x}_{(k)}^T \boldsymbol{A}^T \boldsymbol{P} \boldsymbol{B}_{(k)} \text{sign}\left(s_{(k)}\right) \\ & + \boldsymbol{x}_{(k)}^T \boldsymbol{A}^T \boldsymbol{P} \boldsymbol{\xi}_{(k)} + \boldsymbol{B}_{(k)}^T \boldsymbol{P} \boldsymbol{A} \boldsymbol{x}_{(k)} \text{sign}\left(s_{(k)}\right) \\ & + \boldsymbol{B}_{(k)}^T \boldsymbol{P} \boldsymbol{B}_{(k)} + \boldsymbol{B}_{(k)}^T \boldsymbol{P} \boldsymbol{\xi}_{(k)} \text{sign}\left(s_{(k)}\right) \\ & + \boldsymbol{\xi}_{(k)}^T \boldsymbol{P} \boldsymbol{A} \boldsymbol{x}_{(k)} + \boldsymbol{\xi}_{(k)}^T \boldsymbol{P} \boldsymbol{B}_{(k)} \text{sign}\left(s_{(k)}\right) \\ & + \boldsymbol{\xi}_{(k)}^T \boldsymbol{P} \boldsymbol{\xi}_{(k)}.\end{aligned} \tag{32}$$

Using the Λ inequality [35]

$$\boldsymbol{X}^T \boldsymbol{Y} + \boldsymbol{Y}^T \boldsymbol{X} \leq \boldsymbol{X}^T \boldsymbol{\Lambda} \boldsymbol{X} + \boldsymbol{Y}^T \boldsymbol{\Lambda}^{-1} \boldsymbol{Y} \tag{33}$$

allows for the following terms to be obtained:

$$\begin{aligned}& \boldsymbol{x}_{(k)}^T \boldsymbol{A}^T \boldsymbol{P} \boldsymbol{B}_{(k)} \text{sign}\left(s_{(k)}\right) + \boldsymbol{B}_{(k)}^T \boldsymbol{P} \boldsymbol{A} \boldsymbol{x}_{(k)} \text{sign}\left(s_{(k)}\right) \\ & \leq \boldsymbol{x}_{(k)}^T \boldsymbol{A}^T \boldsymbol{P} \boldsymbol{\Lambda}_1 \boldsymbol{P} \boldsymbol{A} \boldsymbol{x}_{(k)} + \boldsymbol{B}_{(k)}^T \boldsymbol{\Lambda}_1^{-1} \boldsymbol{B}_{(k)} \\ & \boldsymbol{x}_{(k)}^T \boldsymbol{A}^T \boldsymbol{P} \boldsymbol{\xi}_{(k)} + \boldsymbol{\xi}_{(k)}^T \boldsymbol{P} \boldsymbol{A} \boldsymbol{x}_{(k)} \\ & \leq \boldsymbol{x}_{(k)}^T \boldsymbol{A}^T \boldsymbol{P} \boldsymbol{\Lambda}_2 \boldsymbol{P} \boldsymbol{A} \boldsymbol{x}_{(k)} + \boldsymbol{\xi}_{(k)}^T \boldsymbol{\Lambda}_2^{-1} \boldsymbol{\xi}_{(k)} \\ & \boldsymbol{B}_{(k)}^T \boldsymbol{P} \boldsymbol{\xi}_{(k)} \text{sign}\left(s_{(k)}\right) + \boldsymbol{\xi}_{(k)}^T \boldsymbol{P} \boldsymbol{B}_{(k)} \text{sign}\left(s_{(k)}\right) \\ & \leq \boldsymbol{\xi}_{(k)}^T \boldsymbol{P} \boldsymbol{\Lambda}_3 \boldsymbol{P} \boldsymbol{\xi}_{(k)} + \boldsymbol{B}_{(k)}^T \boldsymbol{\Lambda}_3^{-1} \boldsymbol{B}_{(k)}\end{aligned} \tag{34}$$

where $\boldsymbol{\Lambda}_1 = \boldsymbol{\Lambda}_1^T > 0$, $\boldsymbol{\Lambda}_2 = \boldsymbol{\Lambda}_2^T > 0$, and $\boldsymbol{\Lambda}_3 = \boldsymbol{\Lambda}_3^T > 0$.

Then, substituting (34) in (32) results

$$\begin{aligned}\Delta V_{(k)} \leq {} & \boldsymbol{x}_{(k)}^T \left(\boldsymbol{A}^T \boldsymbol{P} \boldsymbol{A} - \boldsymbol{P}\right) \boldsymbol{x}_{(k)} + \boldsymbol{x}_{(k)}^T \boldsymbol{A}^T \boldsymbol{P} \boldsymbol{\Lambda}_1 \boldsymbol{P} \boldsymbol{A} \boldsymbol{x}_{(k)} \\ & + \boldsymbol{B}_{(k)}^T \boldsymbol{\Lambda}_1^{-1} \boldsymbol{B}_{(k)} + \boldsymbol{x}_{(k)}^T \boldsymbol{A}^T \boldsymbol{P} \boldsymbol{\Lambda}_2 \boldsymbol{P} \boldsymbol{A} \boldsymbol{x}_{(k)} \\ & + \boldsymbol{\xi}_{(k)}^T \boldsymbol{\Lambda}_2^{-1} \boldsymbol{\xi}_{(k)} + \boldsymbol{\xi}_{(k)}^T \boldsymbol{P} \boldsymbol{\Lambda}_3 \boldsymbol{P} \boldsymbol{\xi}_{(k)} \\ & + \boldsymbol{B}_{(k)}^T \boldsymbol{\Lambda}_3^{-1} \boldsymbol{B}_{(k)} + \boldsymbol{B}_{(k)}^T \boldsymbol{P} \boldsymbol{B}_{(k)} + \boldsymbol{\xi}_{(k)}^T \boldsymbol{P} \boldsymbol{\xi}_{(k)}.\end{aligned} \tag{35}$$

Equation (35) can be rewritten as

$$\begin{aligned}\Delta V_{(k)} \leq {} & \boldsymbol{x}_{(k)}^T \left\{\boldsymbol{A}^T \left[\boldsymbol{P} + \boldsymbol{P} \left(\boldsymbol{\Lambda}_1 + \boldsymbol{\Lambda}_2\right) \boldsymbol{P}\right] \boldsymbol{A} - \boldsymbol{P}\right\} \boldsymbol{x}_{(k)} \\ & + \boldsymbol{B}_{(k)}^T \left(\boldsymbol{\Lambda}_1^{-1} + \boldsymbol{\Lambda}_3^{-1} + \boldsymbol{P}\right) \boldsymbol{B}_{(k)} \\ & + \boldsymbol{\xi}_{(k)}^T \left(\boldsymbol{\Lambda}_2^{-1} + \boldsymbol{P} \boldsymbol{\Lambda}_3 \boldsymbol{P} + \boldsymbol{P}\right) \boldsymbol{\xi}_{(k)}.\end{aligned} \tag{36}$$

By adding and subtracting $\rho V_{(k)}$ to (36) and rearranging the terms results

$$\begin{aligned}\Delta V_{(k)} \leq {} & \boldsymbol{x}_{(k)}^T \left\{\boldsymbol{A}^T \left[\boldsymbol{P} + \boldsymbol{P} \left(\boldsymbol{\Lambda}_1 + \boldsymbol{\Lambda}_2\right) \boldsymbol{P}\right] \boldsymbol{A} - (1-\rho) \boldsymbol{P}\right\} \boldsymbol{x}_{(k)} \\ & + \boldsymbol{B}_{(k)}^T \left(\boldsymbol{\Lambda}_1^{-1} + \boldsymbol{\Lambda}_3^{-1} + \boldsymbol{P}\right) \boldsymbol{B}_{(k)} \\ & + \boldsymbol{\xi}_{(k)}^T \left(\boldsymbol{\Lambda}_2^{-1} + \boldsymbol{P} \boldsymbol{\Lambda}_3 \boldsymbol{P} + \boldsymbol{P}\right) \boldsymbol{\xi}_{(k)} - \rho V_{(k)}\end{aligned} \tag{37}$$

where $0 < \rho < 1$.

If the LMI

$$\boldsymbol{A}^T \left[\boldsymbol{P} + \boldsymbol{P} \left(\boldsymbol{\Lambda}_1 + \boldsymbol{\Lambda}_2\right) \boldsymbol{P}\right] \boldsymbol{A} - (1 - \rho) \boldsymbol{P} = -\boldsymbol{Q} \tag{38}$$

is feasible for a given $\boldsymbol{Q} = \boldsymbol{Q}^T > 0$, inequality (37) can be rewritten as

$$\begin{aligned}\Delta V_{(k)} \leq {} & - \boldsymbol{x}_{(k)}^T \boldsymbol{Q} \boldsymbol{x}_{(k)} + \boldsymbol{B}_{(k)}^T \left(\boldsymbol{\Lambda}_1^{-1} + \boldsymbol{\Lambda}_3^{-1} + \boldsymbol{P}\right) \boldsymbol{B}_{(k)} \\ & + \boldsymbol{\xi}_{(k)}^T \left(\boldsymbol{\Lambda}_2^{-1} + \boldsymbol{P} \boldsymbol{\Lambda}_3 \boldsymbol{P} + \boldsymbol{P}\right) \boldsymbol{\xi}_{(k)} - \rho V_{(k)}.\end{aligned} \tag{39}$$

Equation (39) can be presented as

$$\Delta V_{(k)} \leq -\boldsymbol{x}_{(k)}^T \boldsymbol{Q} \boldsymbol{x}_{(k)} + \boldsymbol{B}_{(k)}^T \boldsymbol{Z} \boldsymbol{B}_{(k)} + \boldsymbol{\xi}_{(k)}^T \boldsymbol{H} \boldsymbol{\xi}_{(k)} - \rho V_{(k)} \tag{40}$$

where $\boldsymbol{Z} = \boldsymbol{\Lambda}_1^{-1} + \boldsymbol{\Lambda}_3^{-1} + \boldsymbol{P}$ and $\boldsymbol{H} = \boldsymbol{\Lambda}_2^{-1} + \boldsymbol{P} \boldsymbol{\Lambda}_3 \boldsymbol{P} + \boldsymbol{P}$, with $\boldsymbol{Z} = \boldsymbol{Z}^T > 0$ and $\boldsymbol{H} = \boldsymbol{H}^T > 0$.

Considering the following definitions:

$$\begin{aligned}\boldsymbol{x}_{(k)}^T \boldsymbol{Q} \boldsymbol{x}_{(k)} = {} & \left\|\boldsymbol{x}_{(k)}\right\|_Q^2 \\ \boldsymbol{B}_{(k)}^T \boldsymbol{Z} \boldsymbol{B}_{(k)} = {} & \left\|\boldsymbol{B}_{(k)}\right\|_Z^2 \\ \boldsymbol{\xi}_{(k)}^T \boldsymbol{H} \boldsymbol{\xi}_{(k)} = {} & \left\|\boldsymbol{\xi}_{(k)}\right\|_H^2\end{aligned} \tag{41}$$

the following inequalities can be derived:

$$\begin{aligned}& \lambda_{\min}\left(\boldsymbol{Q}\right) \left\|\boldsymbol{x}_{(k)}\right\|^2 \leq \left\|\boldsymbol{x}_{(k)}\right\|_Q^2 \leq \lambda_{\max}\left(\boldsymbol{Q}\right) \left\|\boldsymbol{x}_{(k)}\right\|^2 \\ & \lambda_{\min}\left(\boldsymbol{Z}\right) \left\|\boldsymbol{B}_{(k)}\right\|^2 \leq \left\|\boldsymbol{B}_{(k)}\right\|_Z^2 \leq \lambda_{\max}\left(\boldsymbol{Z}\right) \left\|\boldsymbol{B}_{(k)}\right\|^2 \\ & \lambda_{\min}\left(\boldsymbol{H}\right) \left\|\boldsymbol{\xi}_{(k)}\right\|^2 \leq \left\|\boldsymbol{\xi}_{(k)}\right\|_H^2 \leq \lambda_{\max}\left(\boldsymbol{H}\right) \left\|\boldsymbol{\xi}_{(k)}\right\|^2.\end{aligned} \tag{42}$$

Then, (40) can be rewritten as

$$\begin{aligned}\Delta V_{(k)} \leq {} & - \lambda_{\min}\left(\boldsymbol{Q}\right) \left\|\boldsymbol{x}_{(k)}\right\|^2 + \lambda_{\max}\left(\boldsymbol{Z}\right) \left\|\boldsymbol{B}_{(k)}\right\|^2 \\ & + \lambda_{\max}\left(\boldsymbol{H}\right) \left\|\boldsymbol{\xi}_{(k)}\right\|^2 - \rho V_{(k)}.\end{aligned} \tag{43}$$

By expanding the terms $\|\boldsymbol{B}_{(k)}\|^2$ and $\|\boldsymbol{\xi}_{(k)}\|^2$, it results

$$\begin{aligned}\Delta V_{(k)} \leq {} & - \lambda_{\min}\left(\boldsymbol{Q}\right) \left\|\boldsymbol{x}_{(k)}\right\|^2 \\ & + \lambda_{\max}\left(\boldsymbol{Z}\right) \left[k_1^2 \left|x_{1(k)}\right| + \left(k_2 T_s\right)^2\right] \\ & + \lambda_{\max}\left(\boldsymbol{H}\right) \xi_{1(k)}^2 - \rho V_{(k)}.\end{aligned} \tag{44}$$

Given that $|x_{1(k)}| \leq \|\boldsymbol{x}_{(k)}\|$, (44) can be expressed as

$$\begin{aligned}\Delta V_{(k)} &\leq -\alpha_1 \left\|\boldsymbol{x}_{(k)}\right\|^2 + \alpha_2 \left\|\boldsymbol{x}_{(k)}\right\| + \alpha_3 - \rho V_{(k)} \\ &= -\left(\sqrt{\alpha_1}\left\|\boldsymbol{x}_{(k)}\right\| - \frac{\alpha_2}{2\sqrt{\alpha_1}}\right)^2 + \left(\frac{\alpha_2}{2\sqrt{\alpha_1}}\right)^2 \\ &\quad + \alpha_3 - \rho V_{(k)} \end{aligned} \tag{45}$$

where $\alpha_1 = \lambda_{\min}(\boldsymbol{Q}) > 0$, $\alpha_2 = \lambda_{\max}(\boldsymbol{Z})k_1^2$, and $\alpha_3 = \lambda_{\max}(\boldsymbol{Z})(k_2 T_s)^2 + \lambda_{\max}(\boldsymbol{H})\xi_{1(k)}^2$.

Then,

$$\Delta V_{(k)} \leq c - \rho V_{(k)} \tag{46}$$

where $c = (\frac{\alpha_2}{2\sqrt{\alpha_1}})^2 + \alpha_3$.

Equation (46) can be expressed as

$$V_{(k+1)} \leq (1-\rho) V_{(k)} + c \tag{47}$$

whose solution is given by

$$V_{(k)} \leq (1-\rho)^k V_{(0)} + \sum_{i=0}^{k-1} (1-\rho)^{k-1-i} c \tag{48}$$

and the upper limit can be calculated by

$$\lim_{k\to\infty} V_{(k)} \leq \frac{c}{\rho}. \tag{49}$$

Thus, the convergence radius of the controller is

$$r \leq \frac{c}{\rho}. \tag{50}$$

■

REFERENCES

[1] B. Bilgin, J. Jiang, and A. Emadi, *Switched Reluctance Motor Drives: Fundamentals to Applications*. Boca Raton, FL, USA: CRC Press, 2019.

[2] L. Ge, B. Burkhart, and R. W. De Doncker, "Fast iron loss and thermal prediction method for power density and efficiency improvement in switched reluctance machines," *IEEE Trans. Ind. Electron.*, vol. 67, no. 6, pp. 4463–4473, Jun. 2020.

[3] S. Song, R. Hei, R. Ma, and W. Liu, "Model predictive control of switched reluctance starter/generator with torque sharing and compensation," *IEEE Trans. Transport. Electrific.*, vol. 6, no. 4, pp. 1519–1527, Dec. 2020.

[4] B. Bilgin *et al.*, "Making the case for switched reluctance motors for propulsion applications," *IEEE Trans. Veh. Technol.*, vol. 69, no. 7, pp. 7172–7186, Jul. 2020.

[5] X. D. Xue, K. W. E. Cheng, and S. L. Ho, "Optimization and evaluation of torque-sharing functions for torque ripple minimization in switched reluctance motor drives," *IEEE Trans. Power Electron.*, vol. 24, no. 9, pp. 2076–2090, Sep. 2009.

[6] J. Ye, B. Bilgin, and A. Emadi, "An offline torque sharing function for torque ripple reduction in switched reluctance motor drives," *IEEE Trans. Energy Convers.*, vol. 30, no. 2, pp. 726–735, Jun. 2015.

[7] G. Fang *et al.*, "An intersection-method-based current controller for switched reluctance machines with robust tracking performance," *IEEE Trans. Transport. Electrific.*, vol. 7, no. 4, pp. 2822–2834, Dec. 2021.

[8] G. Fang, F. P. Scalcon, D. Xiao, R. P. Vieira, H. A. Gründling, and A. Emadi, "Advanced control of switched reluctance motors (SRMs): A review on current regulation, torque control and vibration suppression," *IEEE Open J. Ind. Electron. Soc.*, vol. 2, pp. 280–301, 2021, doi: 10.1109/OJIES.2021.3076807.

[9] S. Dhale, B. Nahid-Mobarakeh, and A. Emadi, "A review of fixed switching frequency current control techniques for switched reluctance machines," *IEEE Access*, vol. 9, pp. 39 375–39391, 2021.

[10] F. Peng, J. Ye, and A. Emadi, "A digital PWM current controller for switched reluctance motor drives," *IEEE Trans. Power Electron.*, vol. 31, no. 10, pp. 7087–7098, Oct. 2016.

[11] S. Schulz and K. Rahman, "High-performance digital PI current regulator for EV switched reluctance motor drives," *IEEE Trans. Ind. Appl.*, vol. 39, no. 4, pp. 1118–1126, Jul./Aug. 2003.

[12] S. S. Ahmad and G. Narayanan, "Linearized modeling of switched reluctance motor for closed-loop current control," *IEEE Trans. Ind. Appl.*, vol. 52, no. 4, pp. 3146–3158, Aug. 2016.

[13] X. Li and P. Shamsi, "Inductance surface learning for model predictive current control of switched reluctance motors," *IEEE Trans. Transport. Electrific.*, vol. 1, no. 3, pp. 287–297, Oct. 2015.

[14] X. Li and P. Shamsi,, "Model predictive current control of switched reluctance motors with inductance auto-calibration," *IEEE Trans. Ind. Electron.*, vol. 63, no. 6, pp. 3934–3941, Jun. 2016.

[15] D. F. Valencia, S. R. Filho, A. D. Callegaro, M. Preindl, and A. Emadi, "Virtual-flux finite control set model predictive control of switched reluctance motor drives," in *Proc. 45th Annu. Conf. IEEE Ind. Electron. Soc.*, 2019, vol. 1, pp. 1465–1470.

[16] D. F. Valencia, R. Tarvirdilu-Asl, C. Garcia, J. Rodriguez, and A. Emadi, "A review of predictive control techniques for switched reluctance machine drives. Part I: Fundamentals and current control," *IEEE Trans. Energy Convers.*, vol. 36, no. 2, pp. 1313–1322, Jun. 2021.

[17] Z. Ruiwei, Q. Xisen, J. Liping, Z. Yingchao, Z. Tianwen, and N. Jintong, "An adaptive sliding mode current control for switched reluctance motor," in *Proc. IEEE Conf. Expo Transp. Electrific. Asia-Pac.*, 2014, pp. 1–6.

[18] J. Ye, P. Malysz, and A. Emadi, "A fixed-switching-frequency integral sliding mode current controller for switched reluctance motor drives," *IEEE Trans. Emerg. Sel. Topics Power Electron.*, vol. 3, no. 2, pp. 381–394, Jun. 2015.

[19] K. Hu, J. Ye, J. M. Velni, L. Guo, and B. Yang, "A fixed-switching-frequency sliding mode current controller for mutually coupled switched reluctance machines using asymmetric bridge converter," in *Proc. IEEE Transp. Electrific. Conf. Expo*, 2019, pp. 1–6.

[20] K. Hu, J. Ye, and J. M. Velni, "Sliding mode current control of mutually coupled switched reluctance machines using a three-phase voltage source converter," in *Proc. IEEE Energy Convers. Congr. Expo.*, 2019, pp. 1776–1781.

[21] A. Levant, "Sliding order and sliding accuracy in sliding mode control," *Int. J. Control*, vol. 58, no. 6, pp. 1247–1263, 1993.

[22] T. Gonzalez, J. A. Moreno, and L. Fridman, "Variable gain super-twisting sliding mode control," *IEEE Trans. Autom. Control*, vol. 57, no. 8, pp. 2100–2105, Aug. 2012.

[23] C. L. Baratieri and H. Pinheiro, "New variable gain super-twisting sliding mode observer for sensorless vector control of nonsinusoidal back-EMF PMSM," *Control Eng. Pract.*, vol. 52, pp. 59–69, 2016.

[24] X. Rain, M. Hilairet, and R. Talj, "Second order sliding mode current controller for the switched reluctance machine," in *Proc. 36th Annu. Conf. IEEE Ind. Electron. Soc.*, 2010, pp. 3301–3306.

[25] F. B. Salem, I. Bahri, H. Maamri, and N. Derbel, "A second-order sliding mode control of switched reluctance motor," *Electr. Power Compon. Syst.*, vol. 48, no. 6/7, pp. 640–651, 2020.

[26] H. Gao, F. Salmasi, and M. Ehsani, "Inductance model-based sensorless control of the switched reluctance motor drive at low speed," *IEEE Trans. Power Electron.*, vol. 19, no. 6, pp. 1568–1573, Nov. 2004.

[27] V. Utkin and H. Lee, "Chattering problem in sliding mode control systems," in *Proc. Int. Workshop Variable Struct. Syst.*, 2006, pp. 346–350.

[28] S. Koch and M. Reichhartinger, "Discrete-time equivalents of the super-twisting algorithm," *Automatica*, vol. 107, pp. 190–199, 2019.

[29] H. Kim, M. W. Degner, J. M. Guerrero, F. Briz, and R. D. Lorenz, "Discrete-time current regulator design for ac machine drives," *IEEE Trans. Ind. Appl.*, vol. 46, no. 4, pp. 1425–1435, Jul./Aug. 2010.

[30] I. Salgado, I. Chairez, B. Bandyopadhyay, L. Fridman, and O. Camacho, "Discrete-time non-linear state observer based on a super twisting-like algorithm," *IET Control Theory Appl.*, vol. 8, no. 10, pp. 803–812, 2014.

[31] H. Wang *et al.*, "Precise discrete-time steering control for robotic fish based on data-assisted technique and super-twisting-like algorithm," *IEEE Trans. Ind. Electron.*, vol. 67, no. 12, pp. 10587–10599, Dec. 2020.

[32] H. Li, B. Bilgin, and A. Emadi, "An improved torque sharing function for torque ripple reduction in switched reluctance machines," *IEEE Trans. Power Electron.*, vol. 34, no. 2, pp. 1635–1644, Feb. 2019.

[33] G. Fang, J. Ye, D. Xiao, Z. Xia, X. Wang, and A. Emadi, "Time-efficient torque shaping for switched reluctance machines from linear space," *IEEE Trans. Power Electron.*, vol. 36, no. 8, pp. 9361–9371, Aug. 2021.

[34] J. Taylor, D. F. Valencia, B. Bilgin, M. Narimani, and A. Emadi, "Comparison of current control strategies for low- and high-power switched reluctance motor drives," in *Proc. IEEE Transp. Electrific. Conf. Expo.*, 2020, pp. 198–203.

[35] A. Poznyak, *Advanced Mathematical Tools for Control Engineers: Volume 1: Deterministic Systems*. New York, NY, USA: Elsevier, 2010.

Filipe P. Scalcon (Student Member, IEEE) received the B.S., M.S., and Dr.Eng. degrees in electrical engineering from the Federal University of Santa Maria (UFSM), Santa Maria, Brazil, in 2017, 2019, and 2021, respectively.

He is currently with Power Electronics and Control Research Group (GEPOC), UFSM. His research interests include electrical machine drives, renewable energy conversion, reluctance machines, and digital control.

Gaoliang Fang (Member, IEEE) received the B.S. and M.S. degrees in electrical engineering from Northwestern Polytechnical University (NWPU), Xi'an, China, in 2015 and 2018, respectively. He is currently working toward the Ph.D. degree in electrical engineering with McMaster Automotive Resource Center (MARC), McMaster University, Hamilton, ON, Canada.

His research interests include torque control, vibration and noise reduction of switched reluctance machines, and sensorless control for permanent magnet synchronous machine.

Rodrigo P. Vieira (Member, IEEE) received the B.S. degree from the Universidade Regional do Noroeste do Estado do Rio Grande do Sul (Unijuí), Ijuí, Brazil, in 2007, and the M.Sc. and Dr.Eng. degrees from the Federal University of Santa Maria (UFSM), Santa Maria, Brazil, in 2008 and 2012, respectively, all in electrical engineering.

From 2010 to 2014, he was with the Federal University of Pampa, Alegrete, Brazil. Since 2014, he has been with UFSM, where he is currently a Professor. His research interests include electrical machine drives, sensorless drives, digital control techniques of static converters, and electric vehicles.

Hilton A. Gründling (Member, IEEE) was born in Santa Maria, Brazil, in 1954. He received the B.Sc. degree from the Pontifical Catholic University of Rio Grande do Sul, Porto Alegre, Brazil, in 1977, the M.Sc. degree from the Federal University of Santa Catarina, Santa Catarina, Brazil, in 1980, and the D.Sc. degree from the Technological Institute of Aeronautics, São Paulo, Brazil, in 1995.

Since 1980, he has been with the Federal University of Santa Maria, Rio Grande do Sul, Brazil, where he is currently a Titular Professor. His research interests include robust model reference adaptive control, discrete control, and control system applications.

Ali Emadi (Fellow, IEEE) received the B.S. and M.S. degrees in electrical engineering with highest distinction from the Sharif University of Technology, Tehran, Iran, in 1995 and 1997, respectively, and the Ph.D. degree in electrical engineering from Texas A&M University, College Station, TX, USA, in 2000.

He is currently the Canada Excellence Research Chair Laureate with McMaster University, Hamilton, ON, Canada, and the President and Chief Executive Officer of Enedym Inc. and Menlolab Inc.—two McMaster University spin-off companies. He is also the NSERC/FCA Industrial Research Chair in Electrified Powertrains and Tier I Canada Research Chair in Transportation Electrification and Smart Mobility. He was the Harris Perlstein Endowed Chair Professor of engineering and Director of the Electric Power and Power Electronics Center and Grainger Laboratories, Illinois Institute of Technology, Chicago, where he established research and teaching facilities as well as courses in power electronics, motor drives, and vehicular power systems. He was the Founder, Chairman, and President of Hybrid Electric Vehicle Technologies, Inc. (HEVT)—a university spin-off company of Illinois Tech. He is the principal author/coauthor of more than 500 journal and conference papers as well as several books, including *Vehicular Electric Power Systems* (2003), *Energy Efficient Electric Motors* (2004), *Uninterruptible Power Supplies and Active Filters* (2004), *Modern Electric, Hybrid Electric, and Fuel Cell Vehicles* (2nd ed, 2009), and *Integrated Power Electronic Converters and Digital Control* (2009). He is also the Editor for the *Handbook of Automotive Power Electronics and Motor Drives* (2005) and *Advanced Electric Drive Vehicles* (2014). He is the Co-Editor for *Switched Reluctance Motor Drives* (2018).

Dr. Emadi was the Inaugural General Chair of the 2012 IEEE Transportation Electrification Conference and Expo (ITEC) and has chaired several IEEE and SAE conferences in the areas of vehicle power and propulsion. He was the founding Editor-in-Chief for the IEEE TRANSACTIONS ON TRANSPORTATION ELECTRIFICATION from 2014 to 2020.